J Adv Ceram

Research Article

Data-driven and interpretable machine learning accelerates discovery of $Li_4SrCaSi_2O_8$-based microwave ceramics for high-performance dielectric antennas

Zexu Guo[1], Hongyu Yang[1,✉], Hui Qiao[1], Kui Liu[2], Zhihan Zhang[1], Linzhuang Xing[1], Yihang Li[1,✉], Zhimin Li[1,✉], Yue Hao[3]

Cite this article: Guo Z, Yang H, Qiao H, et al. *J Adv Ceram* 2026, **15**(3): 9221257. https://doi.org/10.26599/JAC.2026.9221257

ABSTRACT: High-performance dielectric antennas have pursued a high quality factor ($Q\times f$) for microwave ceramics. Nevertheless, the cross-laboratory inconsistency in reported $Q\times f$ would confuse the invention of materials systems, owing to divergent preparation and measurement protocols. Herein, based on a self-consistent dataset, an interpretable machine learning framework is proposed to unveil the structure–property relationship and consequently guide the compositional design of candidate microwave ceramic $Li_4SrCaSi_2O_8$. Through feature engineering, nine critical features are identified, in which the Si/Li atomic mass ratio (Si/Li-AW), Si/Sr ionic radius ratio (Si/Sr-IR), and total electronegativity of cations (TEC) are found to be predominant. Interpretability technologies further reveal that a higher Si/Li-AW coupled with lower Si/Sr-IR and TEC is conducive to the increase in the $Q\times f$ value for the chosen decision tree (DT) model. Guided by these insights, Sn^{4+}-doped microwave ceramic $Li_4SrCaSi_{1.98}Sn_{0.02}O_8$ is created with a $Q\times f$ value up to 83,526 GHz, the origin of which is elucidated by P–V–L theory combined with first-principles calculations and infrared spectroscopy. Such an optimized material is ultimately verified by a microstrip patch antenna with a high radiation efficiency of 81.12% and a gain of 5.94 dB in the C-band.

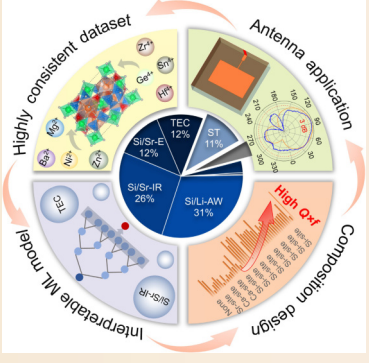

KEYWORDS: microwave ceramic; dielectric properties; dielectric antenna

1 Introduction

As 5G technology and satellite networks enter the microwave frequency band, antennas have become a key bottleneck restricting system performance, directly affecting the data rate and power consumption. Conventional metallic radiators suffer from severe skin effects and surface-wave losses, leading to degraded gain, bulky footprints, and micrometer-level fabrication tolerances. Dielectric antennas avoid the skin-effect limit by replacing conduction currents, making them intrinsically well suited to the microwave band. However, strict requirements should be satisfied for large-scale arrays and handheld terminals. These include a low relative permittivity ($\varepsilon_r < 10$) to suppress surface-wave coupling and feed-line losses, thereby enhancing impedance bandwidth and radiation efficiency, which are critical for high-performance antenna systems [1–7].

Compared with polymer dielectric substrates such as FR-4, low-ε_r ceramics not only possess superior microwave dielectric properties and chemical stability but also withstand harsh operating conditions, including high power, large currents, and extreme thermal cycling, making them particularly suitable for aerospace and high-reliability communication systems. Furthermore, ceramics exhibit high $Q\times f$ values, which significantly enhance antenna radiation efficiency and gain performance [8,9]. Utilizing low-temperature co-fired ceramic (LTCC) technology, these materials can achieve densification sintering at temperatures below 950 °C and can be co-fired with high-conductivity electrodes such as silver or copper, enabling the fabrication of ultrathin, lightweight, and highly integrated manufacturing of antennas [10–12]. Consequently, the development of novel low-ε_r and low-loss microwave ceramics that can be densified at LTCC-compatible temperatures and exhibit good compatibility with electrode materials represents a crucial pathway for achieving breakthroughs in antenna performance [13,14]. $Li_4SrCaSi_2O_8$ (hereafter abbreviated as LSCS) ceramics have attracted much attention due to their low relative permittivity and low dielectric loss. Wang *et al.* [15] achieved a low ε_r value of 7.11 and a high $Q\times f$ value of 41,769 GHz at 1000 °C. Du *et al.* [16] also discovered the low-temperature sinterability of LSCS when synthesized at 900 °C. To achieve

[1] School of Advanced Materials and Nanotechnology, Xidian University, Xi'an 710071, China. [2] School of Information Science and Technology, Southwest Jiaotong University, Chengdu 610031, China. [3] National Key Laboratory of Wide Bandgap Semiconductor Devices and Integrated Technology, Xidian University, Xi'an 710071, China.

✉ Corresponding authors. E-mail: H. Yang, yanghongyu@xidian.edu.cn; Y. Li, liyihang@xidian.edu.cn; Z. Li, zmli@mail.xidian.edu.cn

Received: November 20, 2025; Revised: January 26, 2026; Accepted: January 31, 2026

superior microwave dielectric properties in LSCS-based systems, compositional tailoring via ionic incorporation is urgently needed. Nevertheless, attaining a high $Q\times f$ value through such compositional engineering often struggles to gain broad acceptance. The reproducibility of the reported $Q\times f$ value is undermined by variability in processing routes (e.g., wet-chemical synthesis vs. solid-state reaction), measurement equipment and frequency bands, and testing conditions (e.g., resonant cavity method vs. coaxial transmission/reflection method). Thus, the cross-laboratory consistency of the $Q\times f$ value remains poor, imposing significant constraints on the universal applicability of ion-doping strategies for $Q\times f$ value enhancement.

Recently, the reverse design of material composition and property regulation using machine learning methods has been widely studied, improving the "trial and error" research status [17]. A machine learning model proposed by Qin *et al.* [18] establishes a relationship between the bond length and $Q\times f$ value. This study introduced a machine learning method to establish a $Q\times f$ prediction model with an R^2 value exceeding 0.8 and an root mean square error (RMSE) value below 4000 GHz. The effectiveness of the model is experimentally verified in $(Ba_ySr_{1-y})CuSi_4O_{10}$ ceramics. According to a database of ABO_4-type microwave ceramics, Mo *et al.* [19] used support vector regression with a radial basis function kernel to explore the quantitative structural property relationships of the $Q\times f$ value and establish a prediction model. However, as mentioned, the limited referential value of the $Q\times f$ value from different research groups undoubtedly restrains the prediction accuracy and universal applicability of the model. More importantly, the black-box nature of machine learning models has rarely been revealed, especially at the interpretable mechanism level of the influence of features on the $Q\times f$ value, which hinders the reverse design of ceramics with high $Q\times f$ values.

To address these intertwined challenges of data inconsistency and model interpretability, this work established a closed-loop methodology for the rapid discovery of LSCS-based ceramics with a high $Q\times f$ value. A highly consistent experimental dataset was obtained by synthesizing fifty ion-doped LSCS samples under rigorously controlled conditions. Leveraging interpretable machine learning, key compositional features and synthesis details governing the $Q\times f$ value were identified and validated, moving beyond a black-box prediction. The model's guidance led to the experimental realization of a Sn^{4+}-doped composition with a high $Q\times f$ value. The underlying physical mechanism for the performance enhancement was unraveled through a combination of dielectric theory of complex crystal (P–V–L theory) and first-principles calculations, linking the atomic-scale bonding characteristics to macroscopic dielectric loss. Finally, to bridge the gap between material discovery and functional application, a microstrip patch antenna using the optimized ceramic was designed and fabricated, exhibiting excellent radiation performance. This study not only provides a specific high-performance material for microwave communications but also outlines a generalizable and interpretable framework for accelerating the development of microwave ceramics with a high $Q\times f$ value.

2 Experimental

The overall data-driven workflow of this study for the component design of LSCS microwave ceramics is illustrated in Fig. 1, primarily comprising four parts: dataset construction, feature engineering, model selection and optimization, and interpretability analysis. Initially, a dataset was constructed by adopting fifty ion-doped LSCS ceramic samples and seventeen feature categories, divided into training, validation, and test sets in an 8 : 1 : 1 ratio. After isolating the test set, the synthetic minority oversampling technique (SMOTE) augmentation technique was applied to augment the remaining training and validation subsets [20], where the distributions of samples are presented in Figs. S1 and S2(a) in the Electronic Supplementary Material (ESM). The enhanced sample distribution remains consistent with the original data. Then, feature engineering, including L1 regularization (L1), L2 regularization (L2), relief, gray Relation

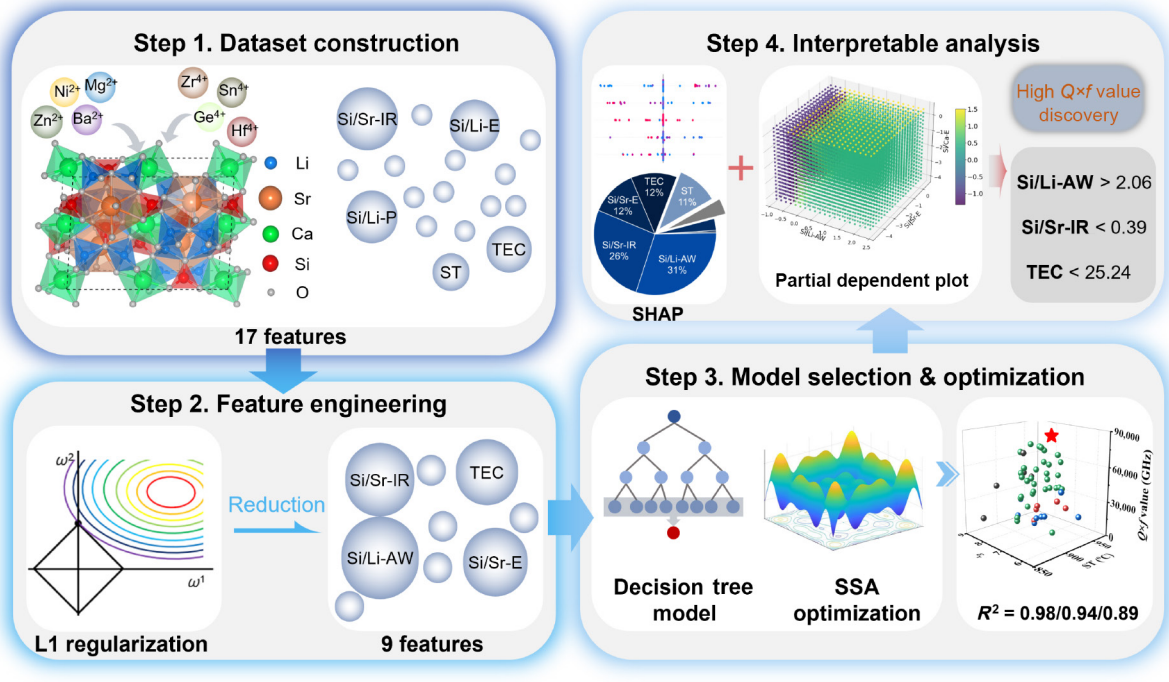

Fig. 1 Schematic illustration of an interpretable framework for $Q\times f$ value prediction of $Li_4SrCaSi_2O_8$ microwave ceramics, where four steps include dataset construction, feature engineering, model selection & optimization, and interpretable analysis.

(Gray), and tree-based model (Tree), was applied to preprocess the data by eliminating redundant and unimportant features. Subsequently, six machine learning algorithms were employed for modeling, including extreme gradient boosting (XGBoost), least squares boosting (LSBoost), back propagation neural network (BPNN), generalized additive model (GAM), decision tree (DT), and random forest (RF). Furthermore, owing to the advantages of strong global search ability, fast convergence speed, good robustness, dynamic update mechanism, and avoiding local optima, the sparrow search algorithm (SSA) was utilized for hyperparameter optimization of the model to obtain the globally optimal predictive model [21]. Building on these steps, interpretability analysis was further conducted on the optimal model to identify optimization directions for enhancing the $Q\times f$ value, thus guiding subsequent material preparation and application research.

2.1 Material preparation and performance test

A series of fifty ion-doped LSCS ceramics was synthesized via the solid-state reaction method, which is listed in Table S1 in the ESM. First, reagent-grade raw powders of Li_2CO_3, $SrCO_3$, $CaCO_3$, and SiO_2 of the main composition were precisely blended according to the designed chemical formula, where divalent oxides containing NiO, ZnO, MgO, and BaO, tetravalent oxides including ZrO_2, GeO_2, HfO_2, and SnO_2, and trivalent and pentavalent oxides covering Al_2O_3, Ta_2O_5, and Nb_2O_5 served as the dopants. Subsequently, the powder mixtures were ball-milled using zirconia media in anhydrous ethanol for 10 h. The blended powders were then dried and passed through an 80-mesh sieve to homogenize the particle size. The sieved powders were calcined at 700 °C for 4 h. The resulting powder was subjected to secondary ball milling for 6 h, followed by drying in an oven at 80 °C. Next, a 50% aqueous acrylic acid solution was added for granulation. Particles of moderate size were selected using 80-mesh sieves and then compressed into cylindrical green bodies measuring 13 mm in diameter and 6 mm in height under 200 MPa pressure. Finally, the green bodies were sintered at 860–960 °C and maintained for 6 h to obtain the LSCS series ceramics.

To characterize and analyze the crystal structure and microwave dielectric properties of LSCS ceramics, a series of testing techniques was employed. The crystal structure was characterized using a powder X-ray diffractometer (XRD; D8 Advance, Bruker, Germany) within the 2θ range of 10°–120°. The micromorphology was observed via a field emission scanning electron microscope (FESEM; SUPRATM55, Zeiss, Germany). A focused ion beam (Helios G4 PFIB, Thermo Fisher, USA) equipped with Xe ion source was used to obtain a finely thinned ceramic sample. A transmission electron microscope (TEM; JEM-F200, JEOL, Japan) equipped with a thermal field emission electron gun and an ultrahigh resolution (UHR) material pole piece was used to analyze the atomic arrangements of the sample, where the acceleration voltage was selected as 200 kV. The energy spectrum (JED-2300T, JEOL, Japan) was used to analyze the distribution of elements.

The bulk density was measured using Archimedes' method. The microwave dielectric properties of the ε_r value and $Q\times f$ value in the frequency range of 8–12 GHz were calculated using the Hakki-Coleman dielectric resonator method with a vector network analyzer (Anritsu MS463228, Japan). The infrared reflectivity spectra covering the far-infrared and mid-infrared bands were measured using a Fourier transform infrared spectrometer (FT-IR; IFS 66v, Bruker, Germany) at the Infrared Spectroscopy and Microscopic Imaging Beam Line Station (BL01B) of the National Synchrotron Radiation Lab of China. The far-infrared spectrum requires air removal from the test chamber before the test to achieve a vacuum test environment. The whole IR spectra were spliced together from the far-infrared and mid-infrared spectra with OPUS software.

The first-principles calculations employed the following parameter settings: Exchange–correlation interactions were described using the Perdew–Burke–Ernzerhof (PBE) functional under the generalized gradient approximation (GGA). Geometric structure optimization was performed using the Broyden–Fletcher–Goldfarb–Shanno (BFGS) algorithm. The valence electron configurations were set as Li($2s^1$), Sr($3s^2$), Ca($3s^2$), Si($2p^4$), and O($2s^22p^4$). The convergence threshold was set at 1.0×10^{-5} eV/atom, the cutoff energy at 571.40 eV, the maximum interatomic force convergence criterion at 0.03 eV/Å, the k-point mesh sampling at 3 × 1 × 1, the maximum stress limit at 0.05 GPa, the maximum atomic displacement limit at 0.001 Å, and the self-consistent field (SCF) calculation convergence accuracy at 1×10^{-6} eV/atom.

2.2 Feature construction

The $Q\times f$ value of fifty well-densified single-phase LSCS microwave dielectric ceramics was assigned as the model's output because extrinsic factors, such as crystallization behavior, porosity, and impurities [22,23], induce frequency dependence in $Q\times f$ values, interfering with $Q\times f$ prediction modeling [24,25]. To apply machine learning methods for investigating the determinants of the $Q\times f$ value and their quantitative contributions, robust feature sets with universality and accessibility were first constructed and are listed in Table S2 in the ESM. The following aspects are considered when constructing the features. The differences in electronegativity affect the nature of the chemical bonds between metal ions and oxygen. The varying electronegativities of Li, Sr, Ca, and Si-site elements lead to the formation of bonds with different polarities. This variation influences the electronic structure. Moreover, the electron transfer from metal ions to oxygen, which is affected by electronegativity differences, impacts the electrical properties. Regarding polarization, the polarizability of metal ions affects the polarization in the bonds formed with oxygen. Ions with higher polarizability are more likely to deform in an electric field, enhancing bond polarity and affecting the dielectric properties of the material. Additionally, ions with higher polarizability led to an uneven distribution of charge within the crystal structure, which in turn affects the symmetry and stability of the crystal. This unevenness may influence the $Q\times f$ value by altering the vibrational modes of the crystal. The radii of different ions also play a significant role in influencing the $Q\times f$ value, as they affect the packing arrangement and structural stability of the crystal. In regard to atomic mass, differences in atomic mass can lead to increased phonon scattering within the lattice. Phonon scattering is one of the primary causes of energy loss, and thus, increased phonon scattering results in a lower $Q\times f$ value. Specifically, ions with greater atomic mass can increase the complexity of lattice vibrational modes, enhancing phonon scattering [26].

3 Results and discussion

3.1 Matching and interpretability analysis of the machine learning model

The development of an effective and interpretable $Q\times f$ prediction model first required the identification of optimal feature selection methods, feature numbers, and model architectures. First, the matching performances are shown in Figs. 2(a1) and 2(a2), where the corresponding mean absolute error (MAE), RMSE, and R^2

values are shown in Fig. S3 in the ESM. In Fig. 2(a1), the matching performances show a distinct difference among the five feature selection methods when using the DT model [27]. The L1 regularization method produces sparse solutions, directly compressing the coefficients of some unimportant features to zero, thus achieving feature selection. In this study, only a portion of the features impact the $Q \times f$ values. L1 regularization reduces model complexity through feature selection, enhancing the model's interpretability and predictive performance [28]. Thus, optimum MAE (4084.89), RMSE (4659.77), and R^2 (0.8961) values on the test set can be achieved. After choosing the L1 method, the performances under different feature numbers are shown in Fig. 2(a2). The regularization strength, denoted as lambda, plays a crucial role in determining the number of coefficients that are reduced to zero. It influences which coefficients remain nonzero. However, it is difficult to precisely select a lambda value that results in exactly seven nonzero coefficients in this study. With an insufficient number of features, the DT model failed to adequately capture the underlying patterns related to the $Q \times f$ value, leading to substantial errors. As the number of features increases to nine, the model's error value reaches its minimum, and R^2 achieves its optimal value. However, a further increase in the feature number

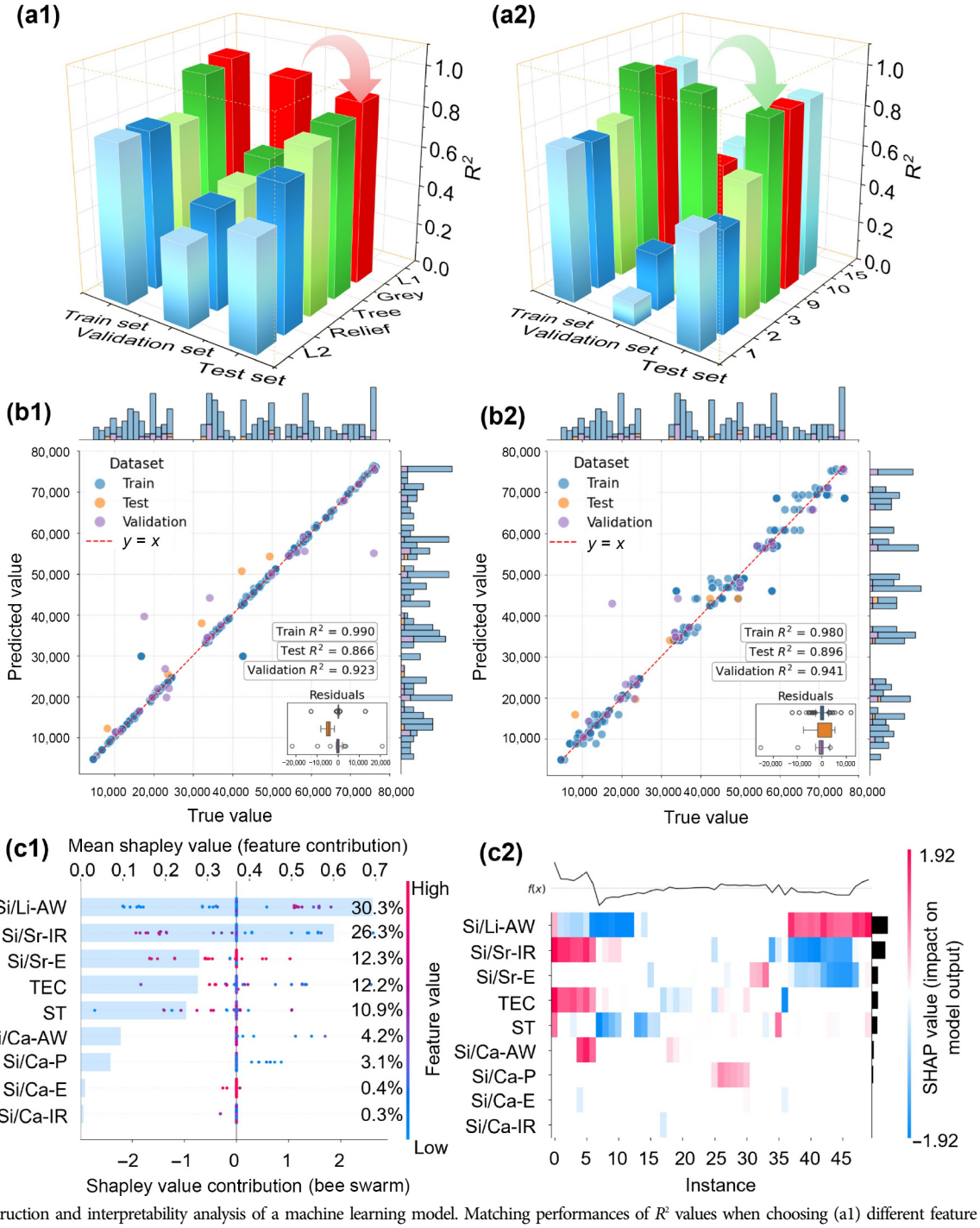

Fig. 2 Construction and interpretability analysis of a machine learning model. Matching performances of R^2 values when choosing (a1) different feature selection methods and (a2) different numbers of features (refer to Fig. S3 in the ESM for complete comparison). (b1) LSBoost model and (b2) DT model. Feature importance and contribution reflected by SHAP analysis: (c1) SHAP swam plot of the nine selected features and (c2) SHAP heatmap.

deteriorates the model's performance, and the R^2 value is unstable, indicating an overfitting risk of the DT model. The dataset containing nine features and the $Q\times f$ value of the LSCS systems is listed in Table S3 in the ESM.

Complex models such as BPNN, RF, and XGBoost models were also employed [29–31], where the comparisons of matching performances are shown in Figs. 2(b1) and 2(b2) and Fig. S4 in the ESM. The BPNN model is prone to becoming trapped in local optima, while the RF and XGBoost models may overfit if there are too many trees. In contrast, the DT model with a simpler structure exhibits stronger adaptability to small datasets with nine features and can effectively capture the relationship between the features and the $Q\times f$ value. In the DT model, relatively fewer hyperparameters are needed, such as tree depth and minimum sample splitting. This enables decision trees to more readily identify the optimal parameter configuration with limited data and features. Other models, however, require a greater number of hyperparameters, including the number of layers and nodes in neural networks and the number of trees and maximum depth in random forests. The performance of models can be significantly compromised if these hyperparameters are not finely tuned. Consequently, the DT model with nine features achieves the optimal fitting performance.

The $Q\times f$ value can be reasonably correlated with nine necessary features using the DT model. Quantifying the contribution and impact of these features on the $Q\times f$ value is essential for elucidating the model's inner workings and defining the material composition criteria for achieving high $Q\times f$ values. To solve this issue, the Shapley additive explanations (SHAP) interpretability technique was used to analyze the importance and interaction effects of features [32]. The variations in Shapley values for different features in different samples are shown in Fig. 2(c1). Color variations reflect the magnitude of SHAP values, with red indicating a positive impact and blue representing a negative impact. The top six most significant features are Si/Li atomic mass ratio (Si/Li-AW), Si/Sr ionic radius ratio (Si/Sr-IR), Si/Sr-E, total electronegativity of cations (TEC), ST, and Si/Ca-AW, making approximately 96.2% contributions. Simultaneously, different features exhibit distinct influence patterns: Higher Si/Li-AW values positively affect $Q\times f$ values, while higher Si/Sr-IR and TEC values demonstrate a significant negative impact. The influence mechanism of Si/Sr-E and ST values on $Q\times f$ values is more complex. Figure 2(c2) displays the exact contribution of each feature to any sample. Taking Si/Li-AW as an example, it is shown that its SHAP value is mainly concentrated at a lower level among the first fifteen samples, while its SHAP value gradually increases in the 15th to 35th samples and achieves the highest value among the remaining samples. Figure S5 in the ESM shows the SHAP value of each feature in sample No. 4, where three features show the largest contributions. As indicated, the base value is the model's prediction value without considering any contributions. When the TEC and Si/Sr-IR features are considered, the base value tends to move in the right direction, while the Si/Li-AW feature pushes the predicted value toward the left. Finally, the predicted $Q\times f$ value in this sample is 39,089.73 GHz.

To identify the tipping point at which each feature affects the $Q\times f$ value, the one-dimensional SHAP plots with LOWESS fitting illustrating the contribution of each feature to the prediction of $Q\times f$ values are presented in Fig. S6 in the ESM. In Fig. S6(a) in the ESM, the feature exhibits a positive contribution to the model prediction when Si/Li-AW > 2.07. The enhancement of the $Q\times f$ value with increasing Si/Li-AW is primarily attributed to the suppression of anharmonic lattice vibration scattering, which consequently reduces the intrinsic dielectric loss. According to Reaney's lattice vibration theory [33], dielectric loss in the microwave frequency range primarily originates from energy dissipation caused by anharmonic interactions of lattice vibrations. When the mass of B-site atoms significantly exceeds that of A-site atoms, it induces substantial separation in vibration frequencies and differences in vibration amplitudes between A-site and B-site ions. This pronounced mass contrast reduces the coupling strength between different vibrational modes, effectively suppressing the phonon-phonon scattering rate. In systematic studies on silicate-based and titanate-based microwave ceramics (e.g., $BaO–TiO_2$ systems), Ohsato observed that introducing heavier ions (e.g., Zr^{4+} and Sn^{4+}) to occupy the B-site constitutes an effective strategy for optimizing the $Q\times f$ value. This is consistent with the aforementioned anharmonic suppression mechanism [34]. Similarly, Chen experimentally confirmed through Zr^{4+} substitution for Ti^{4+} in a $BaTi_4O_9$ ceramic that heavy B-site atoms significantly enhance the $Q\times f$ values [35], further substantiating the critical role of increased Si/Li-AW in reducing lattice anharmonicity and intrinsic loss. In Fig. S6(b) in the ESM, Si/Sr-IR demonstrates a trend opposite to that of Si/Li-AW. The feature exhibits a positive contribution to the $Q\times f$ prediction value only when Si/Sr-IR < 0.389. The effects of the Si/Sr-IR value on the $Q\times f$ value mainly lie in B-site cation ordering and lattice anharmonicity. As the Si/Sr-IR value decreases, the Goldschmidt tolerance factor [36] approaches unity, stabilizing the perovskite structure and promoting long-range B-site ordering, which minimizes defect-induced scattering. Simultaneously, the strengthened B–O bonding and expanded A-site space constrain anharmonic atomic displacements, decreasing the intrinsic dielectric loss [31]. In Fig. S6(d) in the ESM, four tipping points were found, where excessively high TEC values tend to exert a negative contribution to $Q\times f$ predictions, while lower TEC values (< 25.25) are more likely to produce a positive contribution. The pure-phase LSCS material exhibits a TEC value of 25.23. When TEC values exceed 25.25, the electronegativity difference between cations and anions decreases substantially. In Pauling's electronegativity theory [37], the ionicity (f_i) of any chemical bond correlates with the electronegativity difference between cations and anions (denoted as X_A and X_B) (Eq. (1)):

$$f_i = 1 - \exp\left(-\frac{(X_A - X_B)^2}{4}\right) \tag{1}$$

Accordingly, a substantial increase in TEC significantly alters ionicity, inducing notable adjustments in the structure. This alteration enhances the anharmonicity of lattice vibrations and exacerbates phonon scattering loss [38]. The combined effects of these factors increase the intrinsic dielectric loss, ultimately manifested as a reduction in the $Q\times f$ value at the macroscopic level. However, when TEC remains at a low level, it enables fine-tuning of bond ionicity without inducing significant alterations in the crystal structure, reducing the anharmonicity of lattice vibrations. This mechanism represents the primary reason for the positive contribution of low TEC to $Q\times f$ predictions. In Figs. S6(c), S6(e), and S6(f) in the ESM, no tipping points were found, where lower ST values (< 900 °C) exhibited negative contributions to $Q\times f$ predictions, primarily attributed to increased extrinsic losses in ceramics resulting from insufficient densification. Furthermore, the two features Si/Sr-E and Si/Ca-AW show no significant linear correlation with SHAP values, indicating that their influences on model predictions may be more complex or indirect.

Utilizing SHAP for global analysis, insights into the

contributions of key features, the thresholds, and the manner of their impact on the $Q\times f$ value were obtained. To further elucidate the influence patterns of these features and to ascertain any potential interactive effects among them, the interaction effect matrix was calculated using the p value test based on analysis of variance, which was corrected for multiple tests using the Bonferroni correction method, as shown in Fig. S7 in the ESM. Only two feature pairs exhibit strong interactions, including Si/Li-AW & Si/Sr-IR and Si/Li-AW & TEC. To explore the local impact of features on $Q\times f$ predictions, partial dependence plot (PDP) analysis was adopted to examine the influence at different feature value ranges when the interactions were deemed insignificant. However, PDP's reliance on the assumption of variable independence presents limitations and may introduce biases when analyzing features with significant interaction effects. To address this, accumulated local effects (ALE) analysis was selected to evaluate the effects of the feature pairs with strong interactions. Unlike SHAP and PDP, ALE conditions the data distribution within a neighborhood range. This enables ALE to more accurately reflect the true contribution of features to the model, especially in scenarios where features are highly correlated. ALE circumvents the issue of multicollinearity, providing a reliable analysis of feature contributions [39]. As shown in Figs. 3(a1)–3(a3), the linear relationship between features and $Q\times f$ values is primarily manifested along the Si/Li-AW dimension, while the influences of other features remain relatively weak and exhibit nonlinear characteristics. In the three-dimensional partial dependence plots, the impact patterns of features with linear effects are more intuitively demonstrated. From Figs. 3(b1) and 3(b2), it can be observed that the predicted value almost entirely increases monotonically with the rise of Si/Li-AW, while no significant variations are observed along other feature dimensions. Figure 3(b3) indicates that when Si/Li-AW or Si/Ca-AW increases, the predicted value shows an upward trend; however, ST does not demonstrate a clear linear influence on the $Q\times f$ value, which may be attributed to data sparsity within this feature range.

To investigate the pairwise interaction effects among Si/Li-AW, Si/Sr-IR, and TEC, the corresponding second-order ALE plots are presented in Figs. 3(c1) and 3(c2), which can reveal an additional influence beyond the sum of their individual main effects. When Si/Sr-IR and TEC values are low, their interaction pattern with Si/Li-AW exhibits similarity: As long as Si/Sr-IR and TEC remain at low levels, regardless of variations in Si/Li-AW values, the feature interaction consistently exerts a positive influence on $Q\times f$ predictions. However, when Si/Sr-IR values increase, this interaction shifts to a negative impact on $Q\times f$ predictions. Under this condition, increasing Si/Li-AW values can marginally mitigate the negative influence. In contrast, elevated TEC values result in a

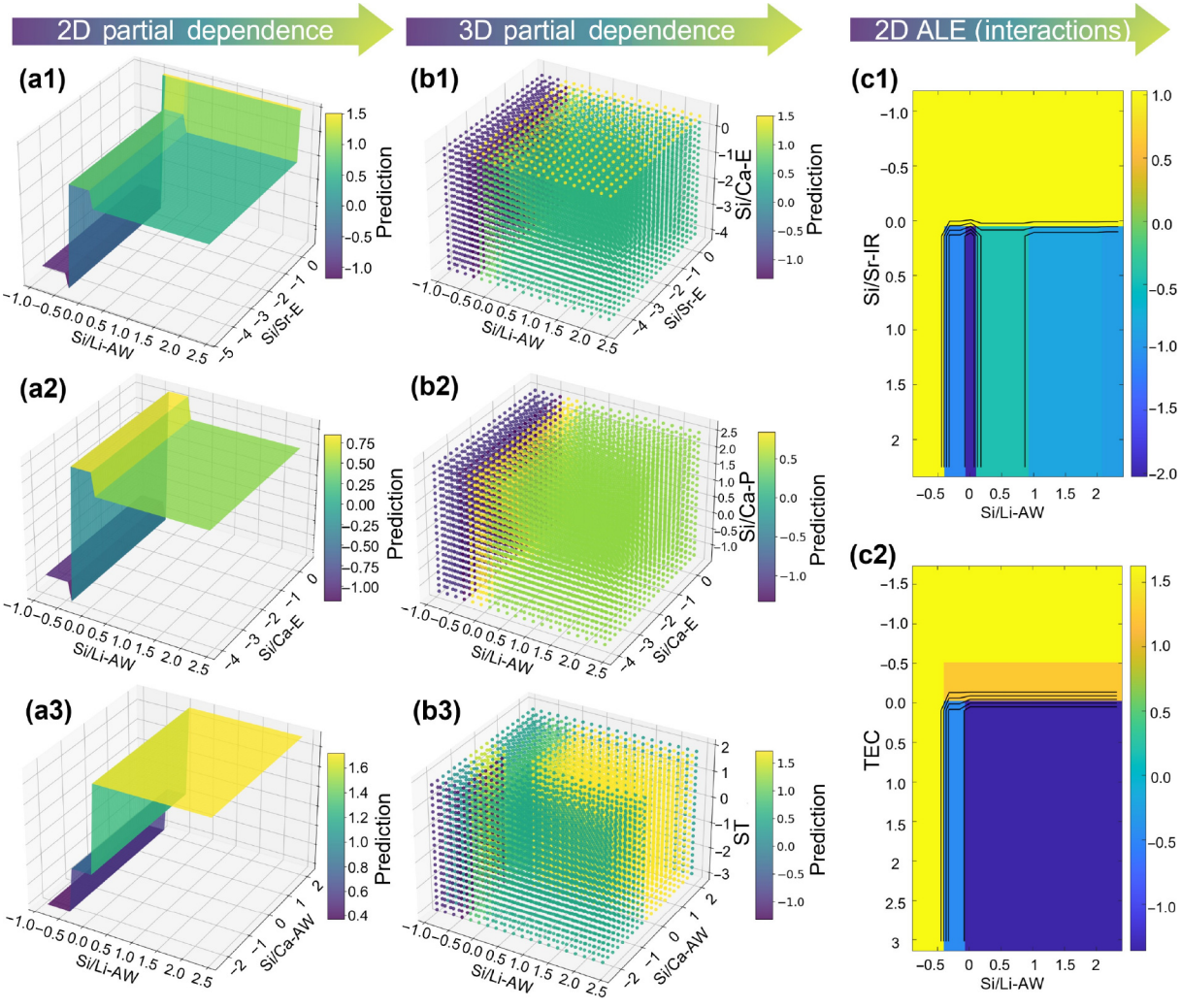

Fig. 3 Synergistic influence of feature pairs on the predicted $Q\times f$ values. (a1–a3) 2D PDP plots for Si/Li-AW & Si/Sr-E, Si/Li-AW & Si/Ca-E, and Si/Li-AW & Si/Ca-AW feature pairs. (b1–b3) 3D PDP plots for Si/Li-AW & Si/Sr-E & Si/Ca-E, Si/Li-AW & Si/Ca-E & Si/Ca-P, and Si/Li-AW & Si/Ca-AW & ST feature pairs. (c1, c2) 2D ALE plots for Si/Li-AW & Si/Sr-IR and Si/Li-AW & TEC feature pairs.

persistently negative impact on $Q\times f$ predictions that remains largely unaltered by changes in Si/Li-AW values. Taken together, the above ALE analysis results provide important references for interpreting $Q\times f$ values in the DT model. When the doped system satisfies the conditions of Si/Li-AW > 2.07, Si/Sr-IR < 0.3875, and TEC < 25.24, higher $Q\times f$ values can be anticipated.

3.2 Experimental validation

Guided by the interpretable model, it was determined that substituting the Si site with heavier isovalent cations is effective for enhancing the $Q\times f$ value. Among common tetravalent dopants (e.g., Zr^{4+}, Ge^{4+}, Hf^{4+}, Sn^{4+}), Sn^{4+} and Hf^{4+} have higher atomic masses, which most significantly increase the Si/Li-AW value. Calculations show that 2 mol% Sn^{4+} substitution ($Li_4SrCaSi_{1.98}Sn_{0.02}O_8$) yields a predicted Si/Li-AW > 2.07, while the Si/Sr-IR and TEC remain well below their respective thresholds, while the feature values for 3 mol% Hf^{4+} substitution ($Li_4SrCaSi_{1.97}Hf_{0.03}O_8$) cannot fully meet the requirement of increasing the $Q\times f$ value. Thus, LSCS-S was selected as the target composition and synthesized. The predicted $Q\times f$ value for $Li_4SrCaSi_{1.97}Hf_{0.03}O_8$ was 69,524 GHz (70,725 for the experimental value), while the predicted $Q\times f$ value of 75,660 GHz for $Li_4SrCaSi_{1.98}Sn_{0.02}O_8$ (83,526 GHz for the experimental value) was close to the predicted value, as listed in Table S3 in the ESM. To investigate the physical mechanism behind the enhancement, this study prepared pure $Li_4SrCaSi_2O_8$ (LSCS-P) ceramics for comparison with Sn^{4+}-ion-doped LSCS-S samples. As shown in Figs. 4(a) and 4(b), the XRD patterns of both sample groups show high agreement with the $Li_4SrCaSi_2O_8$ standard card (JCPDS No. 01-083-0763), confirming their orthorhombic structure. The XRD refinement results of LSCS-S and LSCS-P, including bond lengths, unit cell volumes, and other information, are presented in Table S4 in the ESM. Scanning electron microscopy (SEM) images reveal that the LSCS-S ceramic has a smaller average grain size of 2.3 μm compared to that of the LSCS-P ceramic (~2.57 μm). This reduced grain size increases the number of grain boundaries per unit volume. It is noteworthy that grain boundaries typically contain complex defects, impurities, and varying potential barriers and energy level distributions. Under microwave fields, the energy level structures within these grain boundary regions interact with electromagnetic waves, leading to energy dissipation and significantly enhancing the material's contribution to extrinsic dielectric loss. However, the actual $Q\times f$ value of LSCS-S ceramics is higher, demonstrating its particularly outstanding capability in suppressing other forms of loss.

The dielectric property modulation mechanism can be decoupled into two factors: exogenous and intrinsic. The former originates from microstructural features such as the second phase, interfaces, and pores, while the latter is dominated by the crystal structure and chemical bonding properties, which can be calculated by using the P–V–L theory. Combined with the aforementioned crystal structure parameters and coordination principles of constituent elements in the LSCS series materials, parameters such as ionicity, lattice energy, and bond energy for both LSCS-S and LSCS-P were calculated. The P–V–L theory [40–42] focuses on the resolution of the dielectric properties of binary A_mB_n-type oxide systems. Its core value is to construct a correlation model between microscopic bonding characteristics and macroscopic dielectric properties by analyzing the ionic/covalent properties of chemical bonds as well as lattice and bond energies to provide theoretical support for revealing the dielectric mechanism of materials. Most of the general ceramic materials are complex crystals that do not allow direct application of this theory. Zhang *et al.* [43] developed a method to split polycrystals into binary crystals after considering the atomic ratio in the chemical molecular formula, the spatial configuration of a particular structure, and the type and length of the chemical bonds. In the LSCS structure, the atomic positions are specifically designated as follows: Li ions are situated at the 8e crystallographic site. Both Sr ions and one type of Si ion are located at the 4d site.

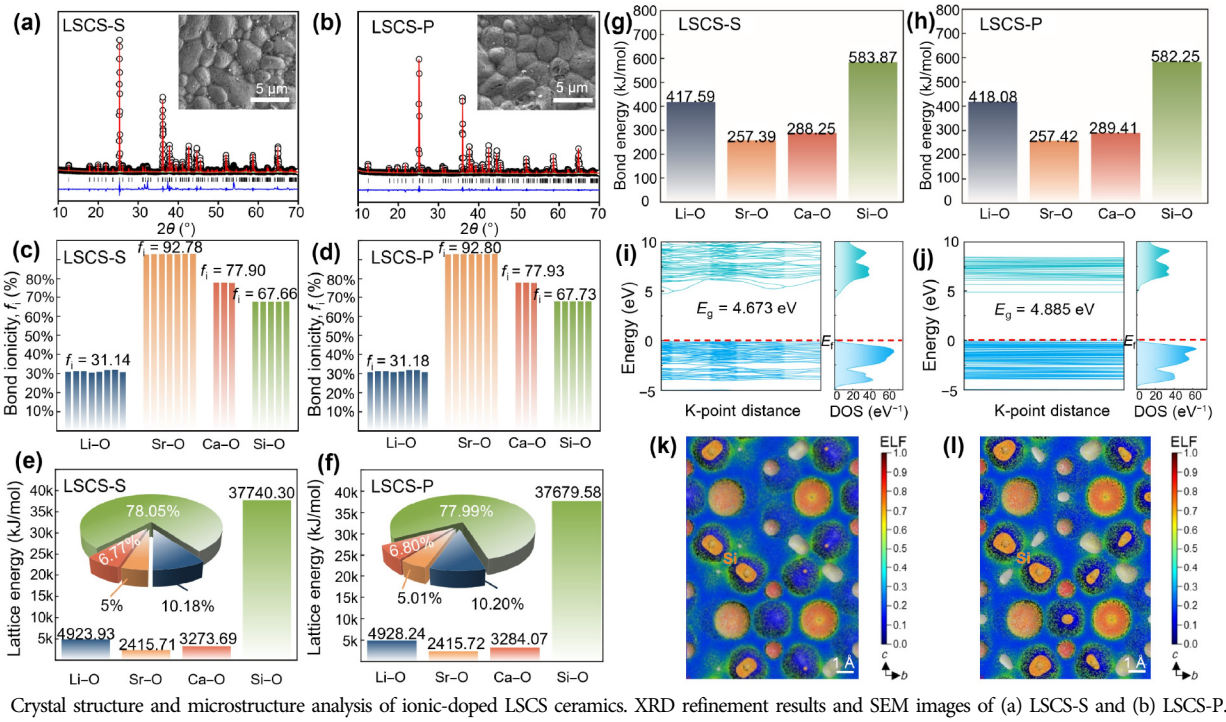

Fig. 4 Crystal structure and microstructure analysis of ionic-doped LSCS ceramics. XRD refinement results and SEM images of (a) LSCS-S and (b) LSCS-P. f_i of chemical bonds in (c) LSCS-S and (d) LSCS-P. Lattice energy (U) of chemical bonds in (e) LSCS-S and (f) LSCS-P. Bond energy (E) of chemical bonds in (g) LSCS-S and (h) LSCS-P. Energy band structure, density of state, and electron localization function of (i, k) LSCS-S and (j, l) LSCS-P.

Ca ions are positioned at the 4b site, while another type of Si ion occupies the 4c site. O ions are categorized into five distinct types, with two types residing at the 4d site. Additionally, there are three types of oxygen ions that are found at the 8e site. The LSCS structural framework is composed of four distinct polyhedral units. Li is tetrahedrally coordinated with four oxygen atoms, creating a [LiO_4] tetrahedron. Sr is encircled by a decahedral arrangement of ten oxygen atoms, resulting in a [SrO_{10}] polyhedron. Ca is octahedrally coordinated with six oxygen atoms, forming a [CaO_6] octahedron. Last, Si is also tetrahedrally coordinated with four oxygen atoms, constituting a [SiO_4] tetrahedron. Considering the bonding environment and valence distribution of LSCS-based ceramics, $Li_4SrCaSi_2O_8$ can be decomposed into a unique binary bonding equation (Eq. (2)):

$$\begin{aligned} Li_4SrCaSi_2O_8 =& Li1_{1/2}O2_{2/5} + Li1_{1/2}O3_{2/5} + Li1_{1/2}O4_{2/5} \\ &+ Li1_{1/2}O5_{2/5} + Li2_{1/2}O1_{2/5} + Li2_{1/2}O3_{2/5} \\ &+ Li2_{1/2}O4_{2/5} + Li2_{1/2}O5_{2/5} + Sr_{1/5}O1_{2/5} \\ &+ Sr_{1/5}O2_{2/5} + Sr_{1/5}O3_{2/5} + Sr_{1/5}O4_{2/5} \\ &+ Sr_{1/5}O5_{2/5} + Ca_{1/3}O3_{2/5} + Ca_{1/3}O4_{2/5} \\ &+ Ca_{1/3}O5_{2/5} + Si1_{1/4}O1_{1/5} + Si1_{1/4}O2_{1/5} \\ &+ Si1_{1/2}O3_{2/5} + Si2_{1/2}O4_{2/5} + Si2_{1/2}O5_{2/5} \end{aligned} \quad (2)$$

where the effective valence electrons for the cations are $Z_{Li} = 1$, $Z_{Sr} = 2$, $Z_{Ca} = 2$, and $Z_{Si} = 4$. The number of effective valence electrons of the O anions relies on the electroneutrality of chemical bonds, which is 3.75, 3, 5, and 15 for Li–O, Sr–O, Ca–O, and Si–O, respectively. It is widely recognized that there is a close connection between the relative permittivity of A_mB_n oxides and the bond ionicity of A–B bonds (Eqs. (3)–(7)):

$$\varepsilon_r = \frac{n^2 - 1}{1 - f_i} + 1 \quad (3)$$

$$f_i = \frac{(C^\mu)^2}{(E_g^\mu)^2} \quad (4)$$

$$(E_g^\mu)^2 = (E_h^\mu)^2 + (C^\mu)^2 \quad (5)$$

$$E_h^\mu = \frac{39.74}{(d^\mu)^{2.48}} \quad (6)$$

$$C^\mu = 14.4 b^\mu \frac{(Z_A^\mu)^* - \frac{n}{m}(Z_B^\mu)^*}{r_0^\mu} e^{(-k_s^\mu r_0^\mu)} \quad (7)$$

where E_g^μ is the average energy gap, including the anisotropic part C^μ and the isotropic part E_h^μ. d^μ is the bond length and r_0^μ is half of the bond length. The Thomas–Fermi shielding effect is expressed through $e^{-k_s^\mu r_0^\mu}$. $(Z_A^\mu)^*$ and $(Z_B^\mu)^*$ refer to the effective valence electrons. The detailed chemical bond characteristics are listed in Table S5 in the ESM. After Sn^{4+} ion doping at the Si site, the TEC value increased from 25.23 to 25.2324. According to Pauling's electronegativity theory, this change indicates a reduction in bond ionicity. The calculation results from the P–V–L theory in Figs. 4(c) and 4(d) further confirm this observation: The introduction of Sn^{4+} leads to decreased ionicity in both Li–O and Si–O bonds. The reduction in bond ionicity implies a more symmetric electron cloud distribution, weakening the ionic displacement polarization capability. On the basis of the Clausius-Mossotti relation, the relative permittivity (ε_r) is closely related to ionic polarizability. Consequently, the decreased ionicity of Li–O and Si–O bonds directly causes a reduction in the overall relative permittivity of the ceramic material, with the ε_r value decreasing from 7.51 for LSCS-P to 7.29 for LSCS-S. Bond ionicity can be further used to calculate the lattice energy (U), which is necessary in characterizing the electrostatic attraction strength between cations and anions in crystals, and its magnitude directly reflects the overall stability of the lattice structure [44,45]. Theoretical studies indicate that an increase in the U value can effectively suppress the amplitude of anharmonic vibrations in the lattice. This reduction in anharmonic vibrations is critical, as it represents one of the primary microscopic sources of intrinsic dielectric loss. Thus, enhanced lattice energy will directly lead to a decrease in intrinsic dielectric loss (Eqs. (8)–(11)):

$$U = \sum\nolimits_\mu U_b^\mu \quad (8)$$

$$U_b^\mu = U_{bc}^\mu + U_{bi}^\mu \quad (9)$$

$$U_{bc}^\mu = 2100 m \frac{(Z_A^\mu)^{1.64}}{(d^\mu)^{0.75}} f_c^\mu \quad (10)$$

$$U_{bi}^\mu = 1270 \frac{(m+n) Z_A^\mu Z_B^\mu}{d^\mu} \left(1 - \frac{0.4}{d^\mu}\right) f_i^\mu \quad (11)$$

where U_b^μ refers to the lattice energies of the bond. m and n are values from A_mB_n binary bonding formula. Z_A^μ and Z_B^μ characterize the effective charge valence states of cations and anions, respectively. U_{bi}^μ and U_{bc}^μ denote the lattice energies from the ionic and covalent parts of the bond, respectively. m and n values were obtained from A_mB_n. The bond contributions to lattice stability can be obtained in Figs. 4(e) and 4(f). The Si–O bond contributes the largest share of the lattice energy, confirming its central role in maintaining lattice stability. In addition, the lattice energy and total lattice energy of Si–O bonds in LSCS-S are larger than those of pure-phase LSCS, and from this point of view, it is confirmed that the LSCS-S ceramics possess lower intrinsic dielectric loss, which leads to the enhancement of the $Q \times f$ value. Thus, ion doping engineering for the Si site to optimize the lattice energy has become an effective strategy to enhance the $Q \times f$ value.

From another perspective, the bond energy (E) of the chemical bonds in polyhedra represents the stability of the polyhedral and affects the $Q \times f$ value of the ceramics [46,47]. The bond energy is related to the bond strength, and the repulsive strength induced by the rotation of the polyhedra increases with increasing bond energy. The bond energy can be analyzed from electronegativity and chemical bonding theory as Eqs. (12)–(14):

$$E = \sum\nolimits_\mu (E_c^\mu t_c + E_i^\mu t_i) \quad (12)$$

$$E_c^\mu = \frac{\sqrt{(R_{cA} + R_{cB})(E_{AA} E_{BB})}}{d^\mu} \quad (13)$$

$$E_i^\mu = \frac{33200}{d^\mu} \quad (14)$$

where E consists of a covalent part E_c^μ and an ionic part E_i^μ. t_c and t_i are the covalent mixing factor and the ionic mixing factor. R_{cA} and R_{cB} refer to the covalent radii, respectively. The calculated results are shown in Figs. 4(g) and 4(h). The larger total E value of LSCS-S becomes one of the reasons for the enhanced $Q \times f$ value of

this ceramic. Building upon the systematic evaluation of bonding parameters using P–V–L theory, it is further revealed that the underlying microphysical mechanisms behind these bonding characteristics are from the electronic structure level. The band structures, total density of states (DOS), and electron localization function (ELF) obtained through first-principles calculations are plotted in Figs. 4(i)–4(l), providing another perspective for understanding the regulatory mechanisms of the $Q\times f$ value. From the analysis of the band structure and DOS shown in Figs. 4(i) and 4(j), it can be observed that Sn^{4+} doping reduced the band gap of LSCS-S by 0.212 eV compared to LSCS-P while simultaneously causing a slight increase in the DOS at the valence band maximum of LSCS-S. Generally, a narrowed band gap combined with an increased valence band DOS implies that electron clouds become more easily delocalized between atoms, and the bonding characteristics tend to exhibit a stronger covalent character. Specifically, an enhanced degree of electron sharing between atoms leads to increased covalency in the material [48,49]. Furthermore, the bonding characteristics can be revealed through ELF analysis [50], where high ELF values correspond to greater electron localization [51]. Observation of the electron localization distribution in the $[SiO_4]$ tetrahedra within the ELF diagrams reveals a significant change in the polarity of Si–O bonds: In Fig. 4(l), the wedge-shaped distribution of high ELF regions indicates that the electron cloud is significantly biased toward the O^{2-} side, whereas in LSCS-S, the electron cloud distribution becomes more rectangular, demonstrating a notable enhancement in the covalency of Si–O bonds, which is consistent with the results of P–V–L theoretical calculations.

Intrinsic losses primarily originate from lattice vibration modes, and since the lattice vibration frequencies predominantly fall within the far-infrared region, far-infrared reflectance spectroscopy is crucial for analyzing the intrinsic dielectric behavior of LSCS materials, which provides evidence for the P–V–L theoretical calculations [52]. By measuring the infrared reflectance spectra and utilizing the following relation, the spectra can be transformed into the complex dielectric function (Eq. (15)):

$$R(\omega) = \left| \frac{\sqrt{\varepsilon(\omega)} - 1}{\sqrt{\varepsilon(\omega)} + 1} \right|^2 \tag{15}$$

where ω refers to the wavenumber. Subsequently, the real ($\varepsilon'(\omega)$) and imaginary ($\varepsilon''(\omega)$) components of the relative permittivity were calculated by employing the Kramers-Kronig relation (Eqs. (16) and (17)) [53]:

$$\varepsilon^*(\omega) = \varepsilon'(\omega) - i\varepsilon''(\omega) \tag{16}$$

$$\varepsilon^*(\omega) = \varepsilon_\infty + \sum_{j=1}^{n} \frac{S_j(\omega_j^2 - \omega^2)}{(\omega_j^2 - \omega^2)^2 + \omega^2\gamma^2} - i\sum_{j=1}^{n} \frac{S_j\omega\gamma_j}{(\omega_j^2 - \omega^2)^2 + \omega^2\gamma^2} \tag{17}$$

where ε_∞ denotes the dielectric constant arising from electronic polarization, n represents the number of phonon modes, and S_j, ω_j, and γ_j correspond to the oscillator strength, eigenfrequency, and damping constant, respectively. Under the condition where $\omega_j >> \omega$, Eqs. (18)–(20) can be derived [54]:

$$\varepsilon'(\omega) = \varepsilon_\infty + \sum_{j=1}^{n} \frac{S_j}{\omega_j^2} \tag{18}$$

$$\varepsilon''(\omega) = \sum_{j=1}^{n} \frac{S_j\omega\gamma_j}{\omega_j^2} \tag{19}$$

$$\tan\delta = \frac{\varepsilon''(\omega)}{\varepsilon'(\omega)} = \sum_{j=1}^{n} \frac{S_j\omega\gamma_j}{\varepsilon'(\omega)\,\omega_j{}^4} \tag{20}$$

After fitting the infrared spectra using the classical Lorentz oscillator model, the measured infrared reflectance spectra, with corresponding real and imaginary parts of the complex dielectric constant, are presented in Figs. 5(a) and 5(b). Well-fitted spectra reveal that the LSCS-S ceramic exhibits an ε_r value of 5.53 and a dielectric loss ($\tan\delta$) of 1.04×10^{-4}, while the LSCS-P ceramic shows $\varepsilon_r = 5.60$ and $\tan\delta = 1.98\times10^{-4}$. The dielectric properties of the two materials tested in the TE_{011} mode (9.59 GHz) are close to the fitted curves, indicating that the dielectric characteristics in the microwave range are primarily dominated by the oscillatory absorption of structural phonons. However, grain boundaries and microdefects introduce external loss, causing discrepancies between the experimental and fitted results. The phonon mode parameter details are listed in Tables S6 and S7 in the ESM. The low-frequency mode observed at 103.24 cm^{-1} in LSCS-P disappears in LSCS-S. This is likely due to local structural distortion introduced by Sn^{4+}, which causes significant broadening of this mode and its subsequent merging into the spectral background. Concurrently, a new vibration mode appears at 475.99 cm^{-1} in LSCS-S, which is attributed to the formation of Sn–O bonds resulting from Sn^{4+} incorporation. These changes collectively indicate that Sn^{4+} doping effectively modulates the lattice vibration properties of the material [52]. For the two ceramic systems, the contribution of electronic polarization to the ε_r value reaches 41%, while the remaining contributions come from the vibration of infrared modes. Detailed contributions of phonon modes to the dielectric properties are shown in Fig. 5(c). Among them, the first mode accounts for over 50% of the dielectric loss, representing the primary source of intrinsic loss in LSCS-based ceramics. Notably, Sn^{4+} doping reduces the contribution of the first mode to the dielectric loss from 76.9% to 54.4%, which is necessary for the reduced dielectric loss in LSCS-S. Through the far-infrared reflectance spectroscopy analysis combined with the aforementioned P–V–L theoretical calculations, it is demonstrated that the prediction direction of the DT model enhances the covalency of Si–O bonds and reduces the intrinsic loss of lattice vibrations, which is effective in achieving an improvement in the $Q\times f$ value of the LSCS-based ceramic.

To confirm the stable and ordered crystal structure of the LSCS-S material, the microstructure was characterized using high-angle annular dark-field scanning transmission electron microscopy (HAADF-STEM) and high-resolution transmission electron microscopy (HRTEM) [55], with the results shown in Fig. 6 and Fig. S8 in the ESM. To investigate the elemental distribution at the microscale, EDS mapping analysis was performed within the grain. The HAADF-STEM image (Fig. 6(a)) and element mapping analysis (Figs. 6(b)–6(e)) indicate that the major elements of Sr, Ca, Sn, and Si exhibit a microscopically homogeneous distribution without apparent segregation. Figures 6(g)–6(i) present the structural characterization analysis of the selected region in Fig. 6(f). Among them, the 3D atomic column intensity map in Fig. 6(g) corresponds to the region within the red box. By simulating the intensity distribution of atomic columns, the 3D arrangement of atoms in the sample can be visually displayed, while Fig. 6(h) more clearly displays the variation in atomic column intensities in this selected region. The atomic arrangement in this area is regular, consistent with the periodic arrangement characteristics of the [301] crystal planes. Multiple measurements along the [040] and [12$\bar{3}$] crystal directions using Digital Micrograph software yielded average interplanar spacings of 0.255 and 0.312 nm, respectively. The corresponding fast Fourier transform (FFT)

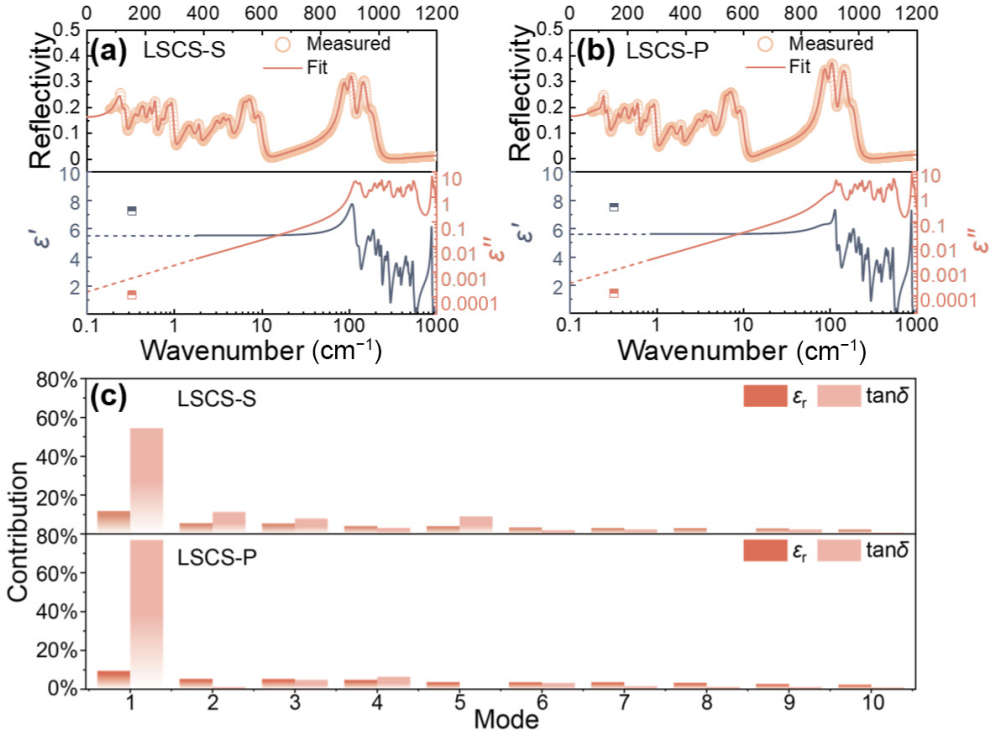

Fig. 5 Intrinsic dielectric property analysis of ionic-doped LSCS ceramics. Measured infrared reflective spectra after fitting, real and imaginary components of the complex dielectric constant of (a) LSCS-S and (b) LSCS-P (red and black squares are the measured ε' and ε'' values under the TE_{011} mode); (c) comparisons of contribution to the dielectric properties from the top ten modes.

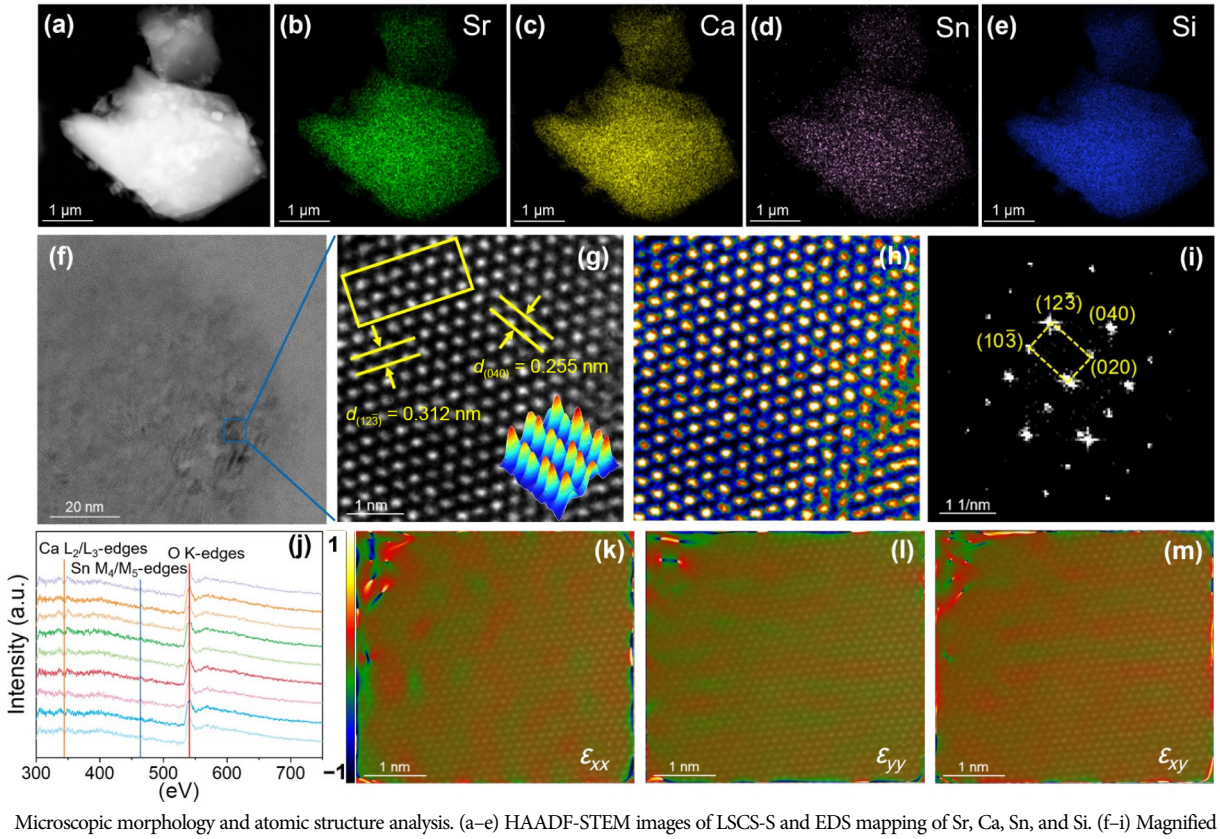

Fig. 6 Microscopic morphology and atomic structure analysis. (a–e) HAADF-STEM images of LSCS-S and EDS mapping of Sr, Ca, Sn, and Si. (f–i) Magnified image viewed along [301] zone axis and its fast Fourier transform pattern. (j) Electron energy loss spectra from different regions in Fig. S8(a) in the ESM. (k–m) Geometric phase analysis of the region in Fig. S8(a) in the ESM.

pattern in Fig. 6(i) matches the XRD analysis results, further confirming that the synthesized modified LSCS-S ceramic possesses a stable and complete LSCS crystal structure.

Electron energy loss spectroscopy (EELS) identifies the types and contents of elements in materials by analyzing the energy lost when incident electrons interact with the sample. The EELS spectra in Fig. 6(j), from top to bottom, correspond to equal-area regions from the grain center to the edge in Fig. S8(a) in the ESM.

The consistent intensity of the Sn M_4/M_5 absorption edges confirms a uniform solid solution of Sn without grain boundary segregation. More importantly, the stable intensity of the O K-edge prepeak near grain boundaries indicates no significant oxygen loss or enrichment at grain edges. These results directly demonstrate the integrity and chemical stability of the material's grain structure, providing strong microstructural evidence for its macroscopically low-loss characteristics [56,57]. Figures 6(k)–6(m) present the geometric phase analysis (GPA) results from Fig. S8(a) in the ESM, showing the distribution maps of the quantitative strain field and lattice rotation field, respectively. This method can transform the lattice distortions in HAADF-STEM or HRTEM images that are difficult to directly quantify into visualized strain and rotation components [58,59]. Among them, ε_{xx} and ε_{yy} represent the tensile strain of the lattice in the horizontal and vertical directions, respectively, while ε_{xy} reflects the angular changes in the lattice caused by shear strain. The color variations in the images represent the magnitude and direction of strain in different regions. The analyzed area is located at the grain edge, and the results show that the strain distribution is uniform in most regions, with only localized strain concentration in the upper left corner. This phenomenon further indicates that the LSCS-S material has a highly stable crystal structure, maintaining good lattice integrity even near the grain boundaries. This also provides evidence for the low-loss characteristics of LSCS-S material. Integrated with theoretical calculations including P–V–L and ELF, along with microstructural characterization results from HAADF-STEM and HRTEM, it has been fully demonstrated that the enhanced covalency of Si–O bonds serves as the key structural optimization mechanism responsible for the excellent microwave dielectric properties (high $Q\times f$ value) in LSCS-S ceramics. The composition optimization strategy proposed via the DT model and its interpretability analysis provides an effective pathway to achieve such covalent enhancement. Consequently, the proposed Sn^{4+}-incorporated LSCS-based ceramics can be synthesized with a high $Q\times f$ value.

3.3 Design and application of microstrip antennas using LSCS-S ceramics

To validate the material's feasibility for antenna applications, a microstrip patch antenna using LSCS-S ceramic as the dielectric

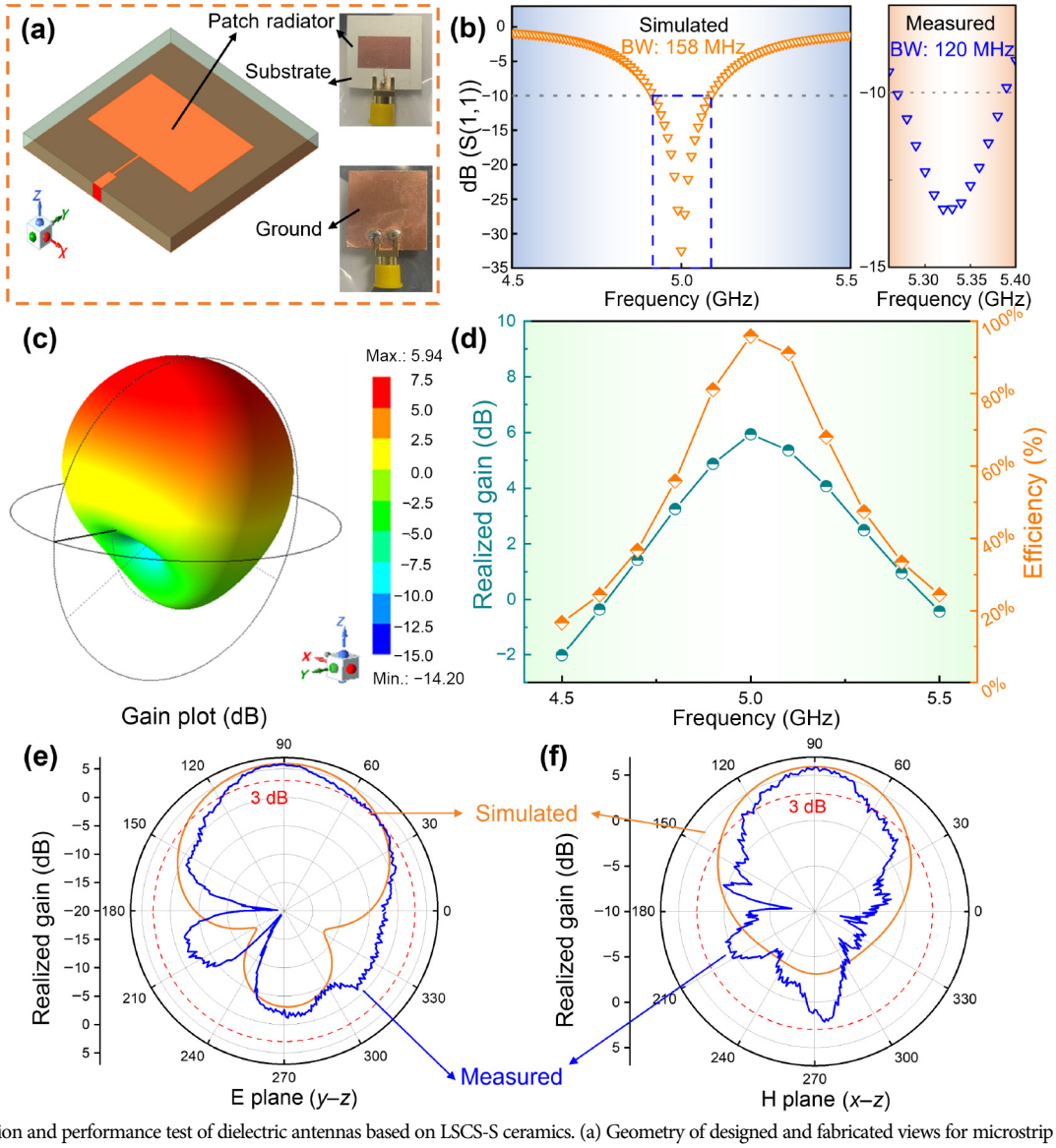

Fig. 7 Simulation and performance test of dielectric antennas based on LSCS-S ceramics. (a) Geometry of designed and fabricated views for microstrip patch antenna. (b) Simulated and measured return loss |S11|. (c) Simulated 3D radiation pattern of antenna. (d) Simulated antenna radiation efficiency and realized gain of antenna. Simulated and measured radiation patterns of (e) E-plane and (f) H-plane.

substrate was further designed and fabricated, with dimensions of 23 mm × 23 mm × 1.6 mm. The antenna structure, physical prototype, and detailed dimensional information are presented in Fig. 7(a) and Table S8 in the ESM. The simulation results indicated an impedance bandwidth of 158 MHz at 5 GHz (Fig. 7(b)), while the measured result was 120 MHz, equivalent to 76% of the simulated value. Regarding the central frequency, the simulated value was 5 GHz, and the measured value was 5.32 GHz. The slight discrepancy between them may be attributed to machining tolerances and fluctuations in the actual dielectric parameters of the substrate [60].

The simulated 3D radiation pattern of the antenna displayed in Fig. 7(c) achieves a maximum gain of 5.94 dB along the *Z*-axis. The gain and radiation efficiency curves (Fig. 7(d)) demonstrate that, owing to the excellent high $Q\times f$ of the LSCS-S material, the antenna maintains a radiation efficiency above 81.12% within the 4.91–5.08 GHz bandwidth, reaching 95.89% at 5 GHz. Figures 7(e) and 7(f) further compare the simulated and measured radiation patterns in the E-plane and H-plane: The simulated and measured 3 dB beamwidths in the E-plane were 96.23° and 77.58°, respectively, while those in the H-plane were 106.63° and 70.71°, respectively. Along the *Z*-axis, the measured maximum gain ranged from 5.83 to 5.88 dB, showing good agreement with the simulated values. Gain deviations in other directions may be caused by machining tolerances, testing environmental interference, and reflections from SMA connectors [61]. The LSCS-S ceramic demonstrates favorable performance as an antenna dielectric substrate with low loss and high gain, proving its potential for applications in C-band (4–8 GHz) microstrip patch antennas.

4 Conclusions

A machine learning model-guided workflow for designing $Li_4SrCaSi_2O_8$ (LSCS)-based microwave dielectric ceramics with a high $Q\times f$ value was demonstrated. By establishing a robust dataset under consistent experimental conditions and employing interpretable machine learning models, key compositional features governing the $Q\times f$ value were identified. The decision tree model outperformed other algorithms in predicting the $Q\times f$ value, with Si/Li-AW, Si/Sr-IR, and TEC being the most critical factors. Experimental validation through Sn^{4+} doping confirmed the model's predictive ability, yielding a high $Q\times f$ value of 83,526 GHz. Structural and electronic analysis revealed that the enhanced performance originated from the increased covalency of Si–O bonds and elevated lattice energy, which suppresses anharmonic lattice vibrations and reduces intrinsic dielectric loss. This was further verified through the intrinsic dielectric properties. Furthermore, the fabricated microstrip antenna using the optimized LSCS-S ceramic exhibited exceptional radiation efficiency and gain, underscoring its suitability for modern communication systems. This study not only advances the understanding of the structure–property relationship in LSCS ceramics but also establishes a generalizable framework for accelerating the discovery of LSCS-based materials for high-performance dielectric antenna applications. However, further investigations on sintering window control and electrode compatibility are necessary to fully assess the LTCC processability of the optimized LSCS-S ceramics.

Acknowledgements

This work was supported by the National Natural Science Foundation of China (No. 62371366), the Key Research and Development Program of Shaanxi (No. 2025CY-YBXM-145), the Central Guiding Local Science and Technology Development Funds of Guizhou (No. 2024-034), and the Xidian University Specially Funded Project for Interdisciplinary Exploration (Nos. TZJHF202515 and TZJH2024063). We thank the staff members of the Infrared spectroscopy and microspectroscopy Beamline (https://cstr.cn/31131.02.HLS. IRSM) at the Hefei Light Source (https://cstr.cn/31131.02. HLS) for providing technical support and assistance in data collection and analysis. We also acknowledge the Instrumental Analysis Center of Xidian University for providing test equipment. Relevant code has been uploaded to a GitHub repository (https://github.com/Westerlywind-ui/LSCS-QF).

Availability of data and materials

The data that support the findings of this study are available from the corresponding author upon reasonable request.

Competing interests

The authors have no competing interests to declare that arerelevant to the content of this article.

Electronic Supplementary Material

Supplementary material is available in the online version of this article at https://doi.org/10.26599/JAC.2026.9221257.

References

[1] Gao F, Zhang KN, Guo YT, *et al.* (Ba,Sr)TiO_3/polymer dielectric composites–progress and perspective. *Prog Mater Sci* 2021, **121**: 100813.

[2] Wang ZW, Guo HH, Huang YY, *et al.* Synergistic dual-phase and microstructure engineering toward temperature-stable, ultra-low loss Li_2TiO_3-based microwave dielectric ceramic. *Adv Funct Mater* 2026, **36**: 18002.

[3] Wang CH, Zhang KH, Bao J, *et al.* Novel temperature-stable (1–*x*) $Ba_3V_2P_3O_{15-x}BaV_2O_6$ composite ceramics with ultralow sintering temperature and low dielectric loss for dielectric resonator antenna applications. *Adv Funct Mater* 2025: 22167.

[4] Huang FY, Su H, Li YX, *et al.* Low-temperature sintering and microwave dielectric properties of $CaMg_{1-x}Li_{2x}Si_2O_6$ (x = 0–0.3) ceramics. *J Adv Ceram* 2020, **9**: 471–480.

[5] Wu FF, Sun RX, Du C, *et al.* P^{5+}-enhanced novel samarium niobate ultralow-loss microwave ceramics as dielectric resonator for X-band antenna applications. *Adv Funct Mater* 2025, **35**: 2421225.

[6] Tian HR, Zhang XH, Zhang ZD, *et al.* Low-permittivity $LiLn(PO_3)_4$ (Ln = La, Sm, Eu) dielectric ceramics for microwave/millimeter-wave communication. *J Adv Ceram* 2024, **13**: 602–620.

[7] Gu ZQ, Pandya S, Samanta A, *et al.* Resonant domain-wall-enhanced tunable microwave ferroelectrics. *Nature* 2018, **560**: 622–627.

[8] Liu YJ, He GQ, Zhang WJ, *et al.* Low loss and temperature-stable $Y_3MgAl_3GeO_{12}$ microwave dielectric ceramics for X-band applications. *J Adv Ceram* 2025, **14**: 9221136–9221148.

[9] Zhang HJ, Dong YJ, Cheng JL, *et al.* Fronthauling for 5G LTE-U ultra dense cloud small cell networks. *IEEE Wirel Commun* 2016, **23**: 48–53.

[10] Xu X, Wu HY. A review on the microwave dielectric ceramics testing technology and related systems. *Adv Ceram* 2025, **46**: 247–285.

[11] Tian HR, Zheng JJ, Liu LT, *et al.* Structure characteristics and microwave dielectric properties of $Pr_2(Zr_{1-x}Ti_x)_3(MoO_4)_9$ solid solution ceramic with a stable temperature coefficient. *J Mater Sci Technol* 2022, **116**: 121–129.

[12] Liu B, Liu J, Hu CC, *et al.* Low-temperature co-fired ceramics with high thermal expansion and reliability for millimeter-wave antennas. *Cell Rep Phys Sci* 2024, **5**: 101959.

[13] Tian HR, Zhang YY, Wang RH, *et al.* Effect of Ge^{4+}-substituted on the structure characteristics and microwave/terahertz dielectric properties of ultra-low ε_r, high $Q\cdot f$ cordierite ceramics. *J Mater Sci Technol* 2025, **216**: 165–177.

[14] Lou WC, Mao MM, Song KX, *et al.* Low permittivity cordierite-based microwave dielectric ceramics for 5G/6G telecommunications. *J Eur Ceram Soc* 2022, **42**: 2820–2826.
[15] Wang HQ, Zhang WJ, Wu Y, *et al.* Novel low temperature co-fired strontium aluminoborate ceramic with low permittivity for microwave applications. *Ceram Int* 2025, **51**: 17311–17317.
[16] Du QB, Wen QZ, Jiang LX, Liu SC, Ma LZ, Li H. A novel low-temperature sintering microwave dielectric ceramic $Li_4SrCaSi_2O_8$ with low-ε_r and low loss. *Ceram Int* 2023, **49**: 22617–22622.
[17] Butler KT, Davies DW, Cartwright H, Isayev O, Walsh A. Machine learning for molecular and materials science. *Nature* 2018, **559**: 547–555.
[18] Qin JC, Liu ZF, Ma MS, *et al.* Structure and microwave dielectric properties of gillespite-type $ACuSi_4O_{10}$ (A = Ca, Sr, Ba) ceramics and quantitative prediction of the $Q\times f$ value via machine learning. *ACS Appl Mater Inter* 2021, **13**: 17817–17826.
[19] Mo LY, Qin JC, Ma MS, *et al.* Machine learning assisted $Q\times f$ value prediction of ABO_4-type microwave dielectric ceramics. *J Materiomics* 2025, **11**: 100926–100936.
[20] Elreedy D, Atiya AF. A comprehensive analysis of synthetic minority oversampling technique (SMOTE) for handling class imbalance. *Inform Sciences* 2019, **505**: 32–64.
[21] Xue JK, Shen B. A novel swarm intelligence optimization approach: Sparrow search algorithm. *Syst Sci Control Eng* 2020, **8**: 22–34.
[22] Gao PX, Liu KY, Wei XL, *et al.* $NaYW_2O_8$: A novel glass-free microwave dielectric ceramic for LTCC application. *Ceram Int* 2023, **49**: 23165–23172.
[23] Kan A, Ogawa H, Ohsato H, Ishihara S. Microwave dielectric properties and crystal structure of $Y_2(Ba_{1-x}Sr_x)(Cu_{1-y}Zn_y)O_5$ solid solutions synthesized by a solid-state reaction method. *Jpn J Appl Phys* 2000, **39**: 5654–5657.
[24] Kamutzki F, Schneider S, Barowski J, Gurlo A, Hanaor D A H. Silicate dielectric ceramics for millimetre wave applications. *J Eur Ceram Soc* 2021, **41**: 3879–3894.
[25] Li L, Chen XM. Frequency-dependent *Qf* value of microwave dielectric ceramics. *J Am Ceram Soc* 2014, **97**: 3041–3043.
[26] Yang HY, Zhang SR, Yang HC, *et al.* Usage of P–V–L bond theory in studying the structural/property regulation of microwave dielectric ceramics: A review. *Inorg Chem Front* 2020, **7**: 4711–4753.
[27] Solorio-Fernández S, Carrasco-Ochoa JA, Martínez-Trinidad JF. A review of unsupervised feature selection methods. *Artif Intell Rev* 2020, **53**: 907–948.
[28] Vidaurre D, Bielza C, Larrañaga P. A survey of L_1 regression. *Int Stat Rev* 2013, **81**: 361–387.
[29] Wang JZ, Wang JJ, Zhang ZG, *et al.* Forecasting stock indices with back propagation neural network. *Expert Syst Appl* 2011, **38**: 14346–14355.
[30] Afanador NL, Smolinska A, Tran TN, *et al.* Unsupervised random forest: A tutorial with case studies. *J Chemometr* 2016, **30**: 232–241.
[31] Qiu YG, Zhou J, Khandelwal M, *et al.* Performance evaluation of hybrid WOA-XGBoost, GWO-XGBoost and BO-XGBoost models to predict blast-induced ground vibration. *Eng Computation* 2022, **38**: 4145–4162.
[32] Alomari Y, Andó M. SHAP-based insights for aerospace PHM: Temporal feature importance, dependencies, robustness, and interaction analysis. *Results Eng* 2024, **21**: 101834–101847.
[33] Reaney IM, Iddles D. Microwave dielectric ceramics for resonators and filters in mobile phone networks. *J Am Ceram Soc* 2006, **89**: 2063–2072.
[34] Ohsato H. Research and development of microwave dielectric ceramics for wireless communications. *J Ceram Soc Jpn* 2005, **113**: 703–711.
[35] Chen YB, Liu SS. Dielectric properties of low Zr-substituted $BaTi_4O_9$ at microwave frequencies. *J Mater Sci: Mater El* 2019, **30**: 5567–5572.
[36] Tsur Y, Dunbar TD, Randall CA. Crystal and defect chemistry of rare earth cations in $BaTiO_3$. *J Electroceram* 2001, **7**: 25–34.
[37] Phillips JC. Ionicity of the chemical bond in crystals. *Rev Mod Phys* 1970, **42**: 317–356.
[38] Cowley RA. The lattice dynamics of an anharmonic crystal. *Adv Phys* 1963, **12**: 421–480.
[39] Apley DW, Zhu JY. Visualizing the effects of predictor variables in black box supervised learning models. *J R Stat Soc B* 2020, **82**: 1059–1086.
[40] Levine BF. Bond susceptibilities and ionicities in complex crystal structures. *J Chem Phys* 1973, **59**: 1463–1486.
[41] Van Vechten JA. Quantum dielectric theory of electronegativity in covalent systems. *I. Eectronic dielectric constant. Phys Rev* 1969, **182**: 891–905.
[42] Phillips JC, Van Vechten JA. Charge redistribution and piezoelectric constants. *Phys Rev Lett* 1969, **23**: 1115–1117.
[43] Wu ZJ, Zhang SY. Semiempirical method for the evaluation of bond covalency in complex crystals. *J Phys Chem A* 1999, **103**: 4270–4274.
[44] Liu DT, Zhang SY, Wu ZJ. Lattice energy estimation for inorganic ionic crystals. *Inorg Chem* 2003, **42**: 2465–2469.
[45] Xiang HC, Zhou Y, Chen JQ, *et al.* Regulation of the temperature stability in ordered olivine microwave dielectric ceramics with low loss for dielectric resonant antenna. *J Adv Ceram* 2025, **14**: 9221149.
[46] Xiao M, Zhang P, Sun HR, *et al.* Influence of Ni^{2+} substitution for Zn^{2+} on microwave dielectric properties of $Zn_{1-x}Ni_xZrNb_2O_8$ ceramics. *J Electron Mater* 2019, **48**: 6553–6560.
[47] Sanderson RT. Electronegativity and bond energy. *J Am Chem Soc* 1983, **105**: 2259–2261.
[48] Phillips JC, Van Vechten JA. Spectroscopic analysis of cohesive energies and heats of formation of tetrahedrally coordinated semiconductors. *Phys Rev B* 1970, **2**: 2147–2160.
[49] Robertson J. Band offsets of wide-band-gap oxides and implications for future electronic devices. *J Vac Sci Technol B* 2000, **18**: 1785–1791.
[50] Shi MG, Ma SY, Xia WS, *et al.* Effects of oxygen vacancy on bond ionicity, lattice energy, and microwave dielectric properties of CeO_2 ceramics with Yb^{3+} substitution. *J Adv Ceram* 2024, **13**: 247–254.
[51] Liu K, Zhang DN, Lei YD, *et al.* Mechanisms affecting microwave dielectric properties of $Li_2Mg_2TiO_5$ ceramics based on lithium excess. *J Alloys Compd* 2024, **1008**: 176717.
[52] Yang HY, Guo ZX, Xiong Z, *et al.* Bond theory, vibrational spectroscopy, and dielectric responses of trirutile ATa_2O_6 (A = Mg, Ni) microwave ceramics. *Ceram Int* 2024, **50**: 19171–19181.
[53] Liu B, Liu XQ, Chen XM. $Sr_2LaAlTiO_7$: A new Ruddlesden–Popper compound with excellent microwave dielectric properties. *J Mater Chem C* 2016, **4**: 1720–1726.
[54] Zhou D, Li WB, Pang LX, *et al.* Abnormal dielectric properties and phase transition in $Bi_{0.783}(Mo_{0.65}V_{0.35})O_4$ scheelite-related structured ceramic. *RSC Adv* 2015, **5**: 19255–19258.
[55] Wang Z, Meng XY, Guo QH, *et al.* Formation and evolution of oxygen vacancy layer in $BaTiO_3$ dielectric ceramics under thermal and electric field stimuli. *Acta Mater* 2025, **299**: 121450.
[56] Sun CL, Liao XB, Xia FJ, *et al.* High-voltage cycling induced thermal vulnerability in $LiCoO_2$ cathode: Cation loss and oxygen release driven by oxygen vacancy migration. *ACS Nano* 2020, **14**: 6181–6190.
[57] Cao N, Chen Z, Zang KT, *et al.* Doping strain induced bi-Ti^{3+} pairs for efficient N_2 activation and electrocatalytic fixation. *Nat Commun* 2019, **10**: 2877.
[58] Wang L, Teng J, Wu Y, *et al.* Size dependence of dislocation activities and independence on theoretical elastic strain limit in Pt nanocrystals revealed by atomic-resolution *in situ* investigation. *Mater Today Nano* 2018, **2**: 1–6.
[59] Biswas K, He JQ, Blum ID, *et al.* High-performance bulk thermoelectrics with all-scale hierarchical architectures. *Nature* 2012, **489**: 414–418.
[60] Roshni SB, Arun S, Sebastian MT, *et al.* Low κ Mg_2SiO_4 ceramic tapes and their role as screen printed microstrip patch antenna substrates. *Mater Sci Eng B* 2021, **264**: 114947.
[61] Xiang HC, Kilpijärvi J, Myllymäki S, *et al.* Spinel-olivine microwave dielectric ceramics with low sintering temperature and high quality factor for 5 GHz Wi-fi antennas. *Appl Mater Today* 2020, **21**: 100826.